Title

Identifying the critical role of li substitution in P2-Na x[LiyNizMn1-y-Z]O2 (0 < x, y, z < 1) intercalation cathode materials for high-energy na-ion batteries

Journal

Chemistry of Materials, 26(2)

ISSN

0897-4756

Authors

Xu, J
Lee, DH
Clément, RJ
et al.

Publication Date

2014-01-28

DOI

10.1021/cm403855t

Peer reviewed

CHEMISTRY OF MATERIALS

Article

pubs.acs.org/cm

Identifying the Critical Role of Li Substitution in P2–$Na_x[Li_yNi_zMn_{1-y-z}]O_2$ ($0 < x, y, z < 1$) Intercalation Cathode Materials for High-Energy Na-Ion Batteries

Jing Xu,[†,⊥] Dae Hoe Lee,[†,⊥] Raphaële J. Clément,[‡] Xiqian Yu,[§] Michal Leskes,[‡] Andrew J. Pell,[∥] Guido Pintacuda,[∥] Xiao-Qing Yang,[§] Clare P. Grey,[‡] and Ying Shirley Meng*[,†]

[†]Department of NanoEngineering, University of California, San Diego, 9500 Gilman Drive, La Jolla, California 92093, United States

[‡]Department of Chemistry, University of Cambridge, Lensfield Road, Cambridge CB2 1EW, United Kingdom

[§]Chemistry Department, Brookhaven National Laboratory, Upton, New York 11973, United States

[∥]Centre de RMN à Très Hauts Champs, Université de Lyon/UMR 5280 CNRS/Ecole Normale Supérieure de Lyon/Université Claude Bernard Lyon 1, 5 rue de la Doua, 69100 Villeurbanne, France

Supporting Information

ABSTRACT: Li-substituted layered P2–$Na_{0.80}[Li_{0.12}Ni_{0.22}Mn_{0.66}]O_2$ is investigated as an advanced cathode material for Na-ion batteries. Both neutron diffraction and nuclear magnetic resonance (NMR) spectroscopy are used to elucidate the local structure, and they reveal that most of the Li ions are located in transition metal (TM) sites, preferably surrounded by Mn ions. To characterize structural changes occurring upon electrochemical cycling, in situ synchrotron X-ray diffraction is conducted. It is clearly demonstrated that no significant phase transformation is observed up to 4.4 V charge for this material, unlike Li-free P2-type Na cathodes. The presence of monovalent Li ions in the TM layers allows more Na ions to reside in the prismatic sites, stabilizing the overall charge balance of the compound. Consequently, more Na ions remain in the compound upon charge, the P2 structure is retained in the high voltage region, and the phase transformation is delayed. Ex situ NMR is conducted on samples at different states of charge/discharge to track Li-ion site occupation changes. Surprisingly, Li is found to be mobile, some Li ions migrate from the TM layer to the Na layer at high voltage, and yet this process is highly reversible. Novel design principles for Na cathode materials are proposed on the basis of an atomistic level understanding of the underlying electrochemical processes. These principles enable us to devise an optimized, high capacity, and structurally stable compound as a potential cathode material for high-energy Na-ion batteries.

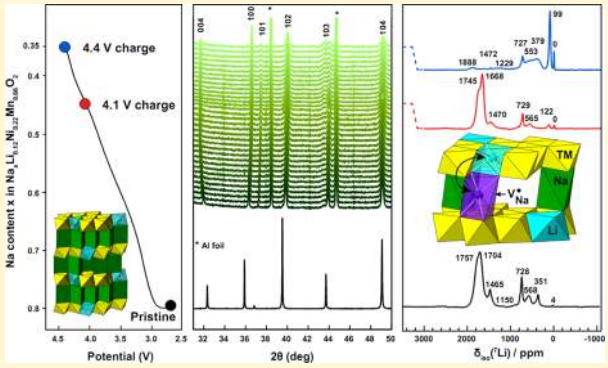

1. INTRODUCTION

The pressing demands for economically accessible and environmentally benign energy storage technologies in large-scale applications are strong drivers for fundamental research in novel materials discovery. Although Li-ion batteries offer the highest energy density among all secondary battery chemistries, concerns regarding lithium availability and its rising cost have driven researchers to investigate sustainable energy-storage alternatives.[1] In this light, Na-ion battery systems have made a major comeback because of the natural abundance and wide distribution of Na resources. Although Li and Na ions share many common features, such as similar valence states and outer shell configurations, the various Na compounds used in batteries have demonstrated unique characteristics resulting in different electrochemical performances. For example, layered $LiCrO_2$ is electrochemically inactive toward Li-ion extraction; however, $NaCrO_2$ can work reversibly as a cathode in rechargeable Na-ion batteries.[2,3] Moreover, the Ti(IV)/Ti(III) redox couple in $Na_2Ti_3O_7$ has shown a surprisingly low average voltage (0.3 V) in Na-ion batteries, which has never been observed in any $Li_xTi_yO_z$-type compound ($x, y, z > 0$).[4,5] Therefore, in-depth insight into the Na-ion electrochemistry is essential as Na-ion intercalation processes exhibit many features in stark contrast to Li-ion electrochemistry.

Among most of the Na cathode compounds reported to date, Na layered oxides with a P2 structure (Na_xTMO_2, TM = transition metal) have drawn significant attention. Their layered structures are able to accommodate large Na-ions and provide spacious diffusion paths as well as structural stability. Research on the structural properties of Na_xTMO_2 started in the 1970s with Delmas et al.,[6,7] who, by studying Na_xCoO_2, demonstrated that Na_xTMO_2 compounds can be used as cathode materials.[8]

Received: November 21, 2013
Revised: December 20, 2013
Published: January 3, 2014

However, limited efforts have been devoted to Na-ion batteries over the past two decades due to the tremendous success of Li-ion batteries. Recently, various P2−Na_xTMO_2 and their binary or ternary derivatives have been extensively investigated, and some of them have demonstrated superior electrochemical performances.[9] Berthelot et al. have reinvestigated P2−Na_xCoO_2 and demonstrated reversible battery performance between $0.45 \leq x \leq 0.90$.[10] It has been shown that P2−$Na_{2/3}[Ni_{1/3}Mn_{2/3}]O_2$ used as cathode in Na cells reversibly exchanges all of the Na ions, leading to a capacity of 160 mAh g^{-1} between 2.0 and 4.5 V.[11,12] Very recently, Yabuuchi et al. reported that $Na_{2/3}[Fe_{1/2}Mn_{1/2}]O_2$ delivers an exceptional initial capacity of 190 mAh g^{-1} between 1.5−4.2 V.[13] However, all of these materials undergo at least one or more phase transformations leading to several voltage steps in their electrochemical profiles. These transformations represent major practical issues for Na-ion batteries because they greatly shorten cycle life and reduce rate capabilities. To address this issue, the Li-substituted P2 compound $Na_{1.0}Li_{0.2}Ni_{0.25}Mn_{0.75}O_2$ was proposed by Kim et al. and displayed a single smooth voltage profile suggesting a solid-solution intercalation reaction.[14] This material delivered 95−100 mAh g^{-1} of specific capacity in the voltage range of 2.0−4.2 V, and demonstrated excellent cycling and rate capabilities. Despite these encouraging improvements, it is still unclear how phase transformations can be prevented and what the critical role of Li is in maintaining the P2 structure.

A comprehensive study on P2−$Na_x[Li_yNi_zMn_{1-y-z}]O_2$ ($0 < x, y, z < 1$) materials is reported in this work. Single smooth voltage profiles are obtained in the voltage range of 2.0−4.4 V along with excellent rate and cycling performances. The crystal structure, including the superlattice formed by partial ordering of the Li, Ni, and Mn ions, is characterized using both X-ray powder diffraction (XRD) and neutron powder diffraction. Because Ni and Mn have similar electron densities, the superlattice formed by ordering of Ni and Mn atoms is difficult to observe by X-ray measurements. Neutron diffraction, however, can distinguish between these elements because the scattering lengths of their most abundant natural isotopes are comparatively different: Ni = 10.3 fm, and Mn = −3.73 fm. While long-range structural information is available from diffraction methods, magic angle spinning (MAS) solid-state NMR provides detailed insight into the local environments experienced by both electrochemically active and inactive ions in the cathode, and can be applied to highly disordered systems. NMR characterization of the ^{7}Li local environments present in the pristine P2−$Na_{0.8}[Li_{0.12}Ni_{0.22}Mn_{0.66}]O_2$ phase and at different stages along the first electrochemical cycle enables us to determine both the electrochemical role of Li in the electrode and the importance of Li substitution in P2 phase stabilization. The structural evolution of the electrode upon charge is tracked by in situ synchrotron XRD (SXRD). X-ray absorption spectroscopy (XAS) is performed to study charge compensation mechanisms. The critical role of Li substitution in phase stabilization is discussed, and novel design principles for this type of P2 materials are presented.

2. EXPERIMENTAL SECTION

2.1. Materials Preparation. The compounds were synthesized using a coprecipitation technique. TM nitrates, $Ni(NO_3)_2{\cdot}6H_2O$ (99%, Acros Organics) and $Mn(NO_3)_2{\cdot}4H_2O$ (98%, Acros Organics), were titrated into a stoichiometric NaOH (Sigma-Aldrich) solution at a rate of 10 mL h^{-1}. Coprecipitated $TM(OH)_2$ was then filtered using a centrifuge, washed three times with deionized water, and then dried at 150 °C for 12 h. Dried $TM(OH)_2$ precursors were ground with a stoichiometric amount of Li_2CO_3 (99.3%, Fisher scientific) and Na_2CO_3 (anhydrous, 99.5%, Strem chemicals) using agate mortar and pestle for 30 min. Precalcination was performed at 500 °C for 5 h in air. The powder was ground again and pressed into pellets. The final calcination process was conducted at 900 °C for 12 h in air. The stoichiometry of the as-synthesized compound was determined by inductively coupled plasma-optical emission spectroscopy (ICP-OES), and the formula of $Na_{0.87}Li_{0.13}Ni_{0.22}Mn_{0.66}O_2$ (normalized to Mn) was confirmed. The presence of excess Na may be caused by a stoichiometric excess in the Na_2CO_3 precursor added during the synthesis.

2.2. Neutron Diffraction. Time of flight (TOF) powder neutron diffraction data were collected on the POWGEN instrument at the Spallation Neutron Source (SNS) in the Oak Ridge National Lab (ORNL). A vanadium container was filled with around 2 g of powder and sent via the mail-in service to the SNS. Data were collected at a wavelength of 1.066 Å to cover a d-spacing range of 0.3−3.0 Å. The histograms were refined using Rietveld refinement with the GSAS software.[15]

2.3. ^{7}Li Nuclear Magnetic Resonance (NMR) Spectroscopy. All ^{7}Li NMR experiments were performed at a magic-angle spinning (MAS) frequency of 60 kHz, using a Bruker 1.3 mm double-resonance HX probe and a recycle delay of 20 ms. ^{7}Li NMR chemical shifts were referenced against solid $^7Li_2CO_3$. Isotropic shifts were extracted by using 2D adiabatic magic angle turning (aMAT)[16] and projection-magic angle turning phase-alternating spinning sideband (pj-MATPASS) experiments,[17] which are adaptations of conventional MAT experiments.[18] The 2D aMAT experiment was performed on as-synthesized P2−$Na_{0.8}[Li_{0.12}Ni_{0.22}Mn_{0.66}]O_2$ on a Bruker Avance III 500 wide-bore spectrometer operating at a ^{7}Li Larmor frequency of −194.6 MHz. The sample temperature was regulated with a flow of N_2 gas (273 K at a flow rate of 1200 l/h) using a Bruker BCU-X. Frequency-swept adiabatic pulses were used to obtain a uniform excitation of the broad ^{7}Li resonances in paramagnetic P2−$Na_{0.8}[Li_{0.12}Ni_{0.22}Mn_{0.66}]O_2$. The aMAT spectrum was obtained using a train of six such π tanh/tan short high-power adiabatic pulses (SHAPs)[19,20] of length 50 μs and sweep width 5 MHz applied at an RF field amplitude of 357 kHz. 2D pj-MATPASS and rotor-synchronized 1D Hahn echo experiments on as-synthesized and cycled P2−$Na_{0.8}[Li_{0.12}Ni_{0.22}Mn_{0.66}]O_2$ samples were recorded at room temperature on a Bruker Avance III 200 wide-bore spectrometer and at a ^{7}Li Larmor frequency of −77.9 MHz. pj-MATPASS and Hahn echo spectra were obtained using $\pi/2$ nonselective pulses of length 0.95 μs at 260 kHz RF field. Each aMAT and pj-MATPASS experiment took between 8 and 13 h. Line shape analysis was carried out using the SOLA line shape simulation package within the Bruker Topspin software and dmfit.[21]

2.4. In Situ Synchrotron X-ray Diffraction (XRD). High-quality XRD patterns were continuously collected in transmission mode at the X14A beamline of the National Synchrotron Light Source (NSLS) using a linear position sensitive silicon detector. Customized coin cells with holes on both sides and covered with Kapton tape were used for in situ measurement at a wavelength of 0.7784 Å. XRD patterns were collected between 4.9° and 41.0° in 2θ angles. The data collection time for each XRD scan was 10 min. Rietveld refinement of the XRD data was carried out using the FullProf software package.

2.5. X-ray Absorption Spectroscopy (XAS). X-ray absorption spectroscopy experiments were performed at the X11B beamline of the National Synchrotron Light Source (NSLS) at Brookhaven National Laboratory. Electrode samples were washed using battery grade diethylene carbonate (DEC) three times. Higher harmonics in the X-ray beam were minimized by detuning the Si (111) monochromator by 40% at the Ni K-edge (8333 eV) and at the Mn K-edge (6539 eV). Transmission spectra were collected along with a simultaneous spectrum on a reference foil of metallic Ni and Mn to ensure consistent energy calibration. Energy calibration was carried out using the first derivative of the spectra of the Ni and Mn metal foils.

The data were analyzed and refined using the Ifeffit[22] and Horae[23] packages.

2.6. Electrochemical Characterization. Cathode electrodes were prepared by mixing 85 wt % $Na_{0.8}[Li_{0.12}Ni_{0.22}Mn_{0.66}]O_2$ with 10 wt % acetylene black (Strem chemicals) and 5 wt % polytetrafluoroethylene (PTFE). Na metal (Sigma-Aldrich) was used as the counter electrode. 1 M $NaPF_6$ (99%, Stremchemicals) dissolved in a 2:1 mixture of battery grade DEC and ethylene carbonate (EC) (Novolyte) was used as the electrolyte, and the glass fiber GF/D (Whatman) was used as the separator. Swagelok type batteries were assembled in an Ar-filled glovebox (H_2O < 0.1 ppm) and tested on an Arbin battery cycler in galvanostatic mode.

3. RESULTS AND DISCUSSION

3.1. Electrochemical Performances of $Na_{0.80}[Li_{0.12}Ni_{0.22}Mn_{0.66}]O_2$. The theoretical capacity of P2−$Na_{0.8}[Li_{0.12}Ni_{0.22}Mn_{0.66}]O_2$ is 118 mAh g^{-1}, considering the Ni^{2+}/Ni^{4+} redox reaction associated with 0.44 mol of Na ions. As shown in Figure 1a, the material exhibits 133 mAh g^{-1} capacity after the first charge, which is 15 mAh g^{-1} higher than the theoretical value, presumably due to electrolyte decomposition and the formation of a solid electrolyte interphase.[24] Starting from the second cycle, the electrochemical profiles of the subsequent 30 cycles almost completely overlap and reveal that about 115 mAh g^{-1} of specific capacity is obtained reversibly. Even up to the 50th cycle, capacity retention is still as high as 91% without any optimization of the electrodes via, for example, carbon coating, nanoscale fabrication, and the use of electrolyte additives. More importantly, the voltage profile displays a smooth curve between 2.0 and 4.4 V for both charge and discharge, indicating that intercalation proceeds via a solid-solution mechanism. Similar phenomena have been observed for the compound $Na_{1.0}Li_{0.2}Ni_{0.25}Mn_{0.7}$ by Kim et al.[24] On the contrary, it has been reported that the structural analogue, P2 −$Na_{2/3}[Ni_{1/3}Mn_{2/3}]O_2$, displays multiple intermediate phases and a phase transformation in the voltage range of 2.0−4.5 V.[25] Therefore, it is speculated that the presence of Li in $Na_{0.80}[Li_{0.12}Ni_{0.22}Mn_{0.66}]O_2$ plays a crucial role in the electrochemical reaction mechanism. We further investigate the location and effect of Li substitution via in situ SXRD and ex situ NMR in later sections. Superior rate performance has been obtained and is illustrated in Figure 1b. The electrode delivers 105.6 mAh g^{-1}at *C*/2, 101.5 mAh g^{-1} at 1*C*, 84.9 mAh g^{-1} at 2*C*, corresponding to 72% of the theoretical capacity, and 70.8 mAh g^{-1} at 5*C*, 60% of the theoretical value.

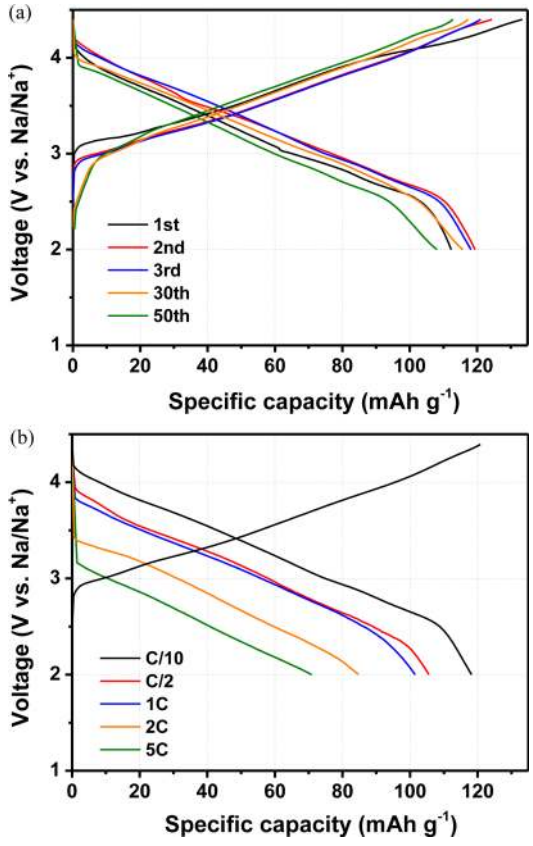

Figure 1. (a) Electrochemical profiles of $Na_{0.80}[Li_{0.12}Ni_{0.22}Mn_{0.66}]O_2$ during the 1st, 2nd, 3rd, 30th, and 50th cycles, and (b) its rate capability at different current densities from *C*/10 to 5*C* (calculated on the basis of a a theoretical capacity of 118 mAh g^{-1}).

3.2. Structural Characterization by Neutron Diffraction and NMR Spectroscopy. Long- and short-range structural properties of as-synthesized $Na_{0.80}[Li_{0.12}Ni_{0.22}Mn_{0.66}]O_2$, such as the formation of superlattice structures and the Li-ion local environments, were investigated using XRD, neutron diffraction, and ^{7}Li solid-state NMR spectroscopy. All of the XRD peaks (Figure S1(a), Supporting Information) could be indexed using the space group $P6_3/mmc$, and refinement results are listed in Table S2 (Supporting Information). Figure 2a shows the neutron diffraction pattern along with the Rietveld refinement. The inset presents a magnified view of the 2.0−2.25 Å region and clearly demonstrates the presence of superstructure. The Miller indices of the peaks indicating Ni/Mn ordering on a $\sqrt{3}a \times \sqrt{3}a$ superlattice are (020), (021), (121), and (122); these are technically "systematically absent" when using the "small hexagonal" model with cell length *a* ($P6_3/mmc$). Previous work on $LiNi_{1/2}Mn_{1/2}O_2$ and $Na_{2/3}Ni_{1/3}Mn_{2/3}O_2$ layered materials has demonstrated that Ni/Mn ordering in the TM layer can be described by a "honeycomb" lattice.[26,27] Therefore, a "large hexagonal" model ($P6_3$) of the TM superlattice, with a $\sqrt{3}a \times \sqrt{3}a$ unit cell (where *a* is the cell parameter of the material with no cation ordering), is used to fit the diffraction patterns.[26] In this model, three different TM positions at (0, 0, 0), (1/3, 2/3, 0), and (1/3, 2/3, 1/2) are present. The refined coordinates of all atoms, and their site occupancies in the large hexagonal model, are given in Table S1 (Supporting Information). The inset of Figure 2a indicates that (020) and (021) peaks are present, although we were not able to obtain a good fit of their intensities. This indicates that there is Li/Ni/Mn ordering in the TM layer but XRD is unable to capture all of the details even in the large hexagonal cell model. Solid-state NMR experiments were therefore performed to investigate the short-range structure.

Li-ion local environments in the pristine P2−$Na_{0.8}[Li_{0.12}Ni_{0.22}Mn_{0.66}]O_2$ phase were studied using ^{7}Li MAS NMR spectroscopy. ^{23}Na MAS NMR experiments were also performed, and the results will be presented in a separate publication. The ^{7}Li resonance frequency of a Li ion surrounded by Ni^{2+} and Mn^{4+} ions is mainly affected by the Fermi contact interaction specific to the TM configuration around the observed nucleus.[28] Both pseudocontact and quadrupolar contributions to the ^{7}Li resonance frequency can be considered negligible as compared to the much larger hyperfine interactions.[28,29] A 2D aMAT experiment was performed to resolve the multiple resonances of the ^{7}Li sites. The 2D spectrum is plotted in Figure 2b along with 1D

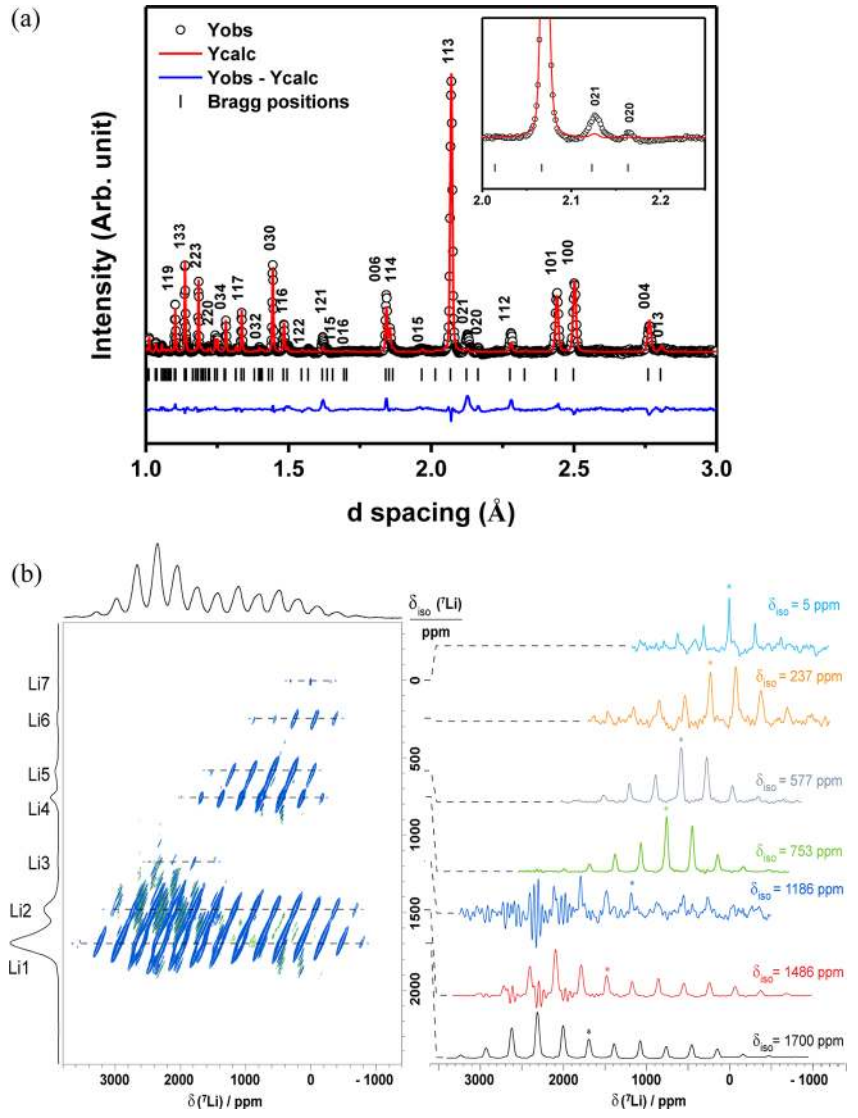

Figure 2. (a) Neutron diffraction patterns, including an extended view of the superlattice region (inset), and (b) the ^{7}Li aMAT NMR spectrum of as-synthesized P2–$Na_{0.80}[Li_{0.12}Ni_{0.22}Mn_{0.66}]O_2$ recorded at 500 MHz. In (b), the 1D double adiabatic spin echo (DASE) spectrum and the F1 sum spectrum are projected at the top and on the left-hand side of the 2D spectrum, respectively. Slices taken in the F2 dimension, centered about the ^{7}Li isotropic shifts, are shown on the right-hand side.

projections from ^{7}Li double adiabatic spin echo (DASE) experiment (top) and a sum projection of the isotropic dimension (left). At least seven ^{7}Li isotropic shifts are clearly observed at 5, 237, 577, 753, 1186, 1486, and around 1700 ppm in the F1 sum spectrum, and their corresponding sideband manifolds are plotted on the right.

On the basis of a previous ^{6}Li NMR study of Li_2MnO_3,[29] we can assign the resonances of Li_1 (ca. 1700 ppm), Li_2 (1486 ppm), and Li_3 (1186 ppm) to Li sites in a honeycomb-like arrangement within the TMO_2 layer. By analogy with our results for Li_2MnO_2–$Li(NiMn)_{0.5}O_2$ "lithium-excess" materials,[30] we further assign Li_1 to Li ions surrounded by 6 nearest neighbor Mn^{4+}, and Li_2 to 5 Mn^{4+} and 1 Ni^{2+}. The 1D Hahn echo spectrum collected on the pristine material (Figure S5, Supporting Information) reveals that the Li_1 resonance results from the overlap of signals from two distinct Li environments with isotropic shifts at ca. 1760 and 1700 ppm. Inhomogeneous broadening of the aMAT spectrum, likely due to a combination of anisotropic bulk magnetic susceptibility (ABMS) effects, temperature gradients across the sample at 60 kHz MAS, and structural disorder, leads to significant broadening of the 1700 ppm peak, so as to inhibit the resolution of the neighboring peak at ca. 1760 ppm. Ab initio and experimentally derived TM–(O–)Li bond pathway contributions for Li-ions in octahedral environments in the TMO_2 layer are in good agreement with these general trends and will be discussed in a future publication.

Cabana et al. have studied the T2/O2 ion-exchanged $Li_{0.67}Ni_{0.33}Mn_{0.67}O_2$ compound, and following their findings we assign Li_4 (753 ppm) and Li_5 (577 ppm) resonances to octahedrally distorted sites in the Na layer.[31] A greater concentration of Ni in the first coordination shell of Li_5 may account for its lower shift as compared to that of Li_4 (by analogy with related Li phases[30]).

As the main lithium resonance in T2/O2 ion-exchanged $Li_{0.67}Ni_{0.33}Mn_{0.67}O_2$ appears at 370 ppm, we can assign Li_6 (237 ppm) and Li_7 (5 ppm) to tetrahedrally distorted sites in the Na layer, occurring as small defects in the ideal structure. The difference in O-layer stacking (P2 vs O2/T2) may account for the discrepancy in Li shifts in the two materials. The relatively

dx.doi.org/10.1021/cm403855t | Chem. Mater. 2014, 26, 1260–1269

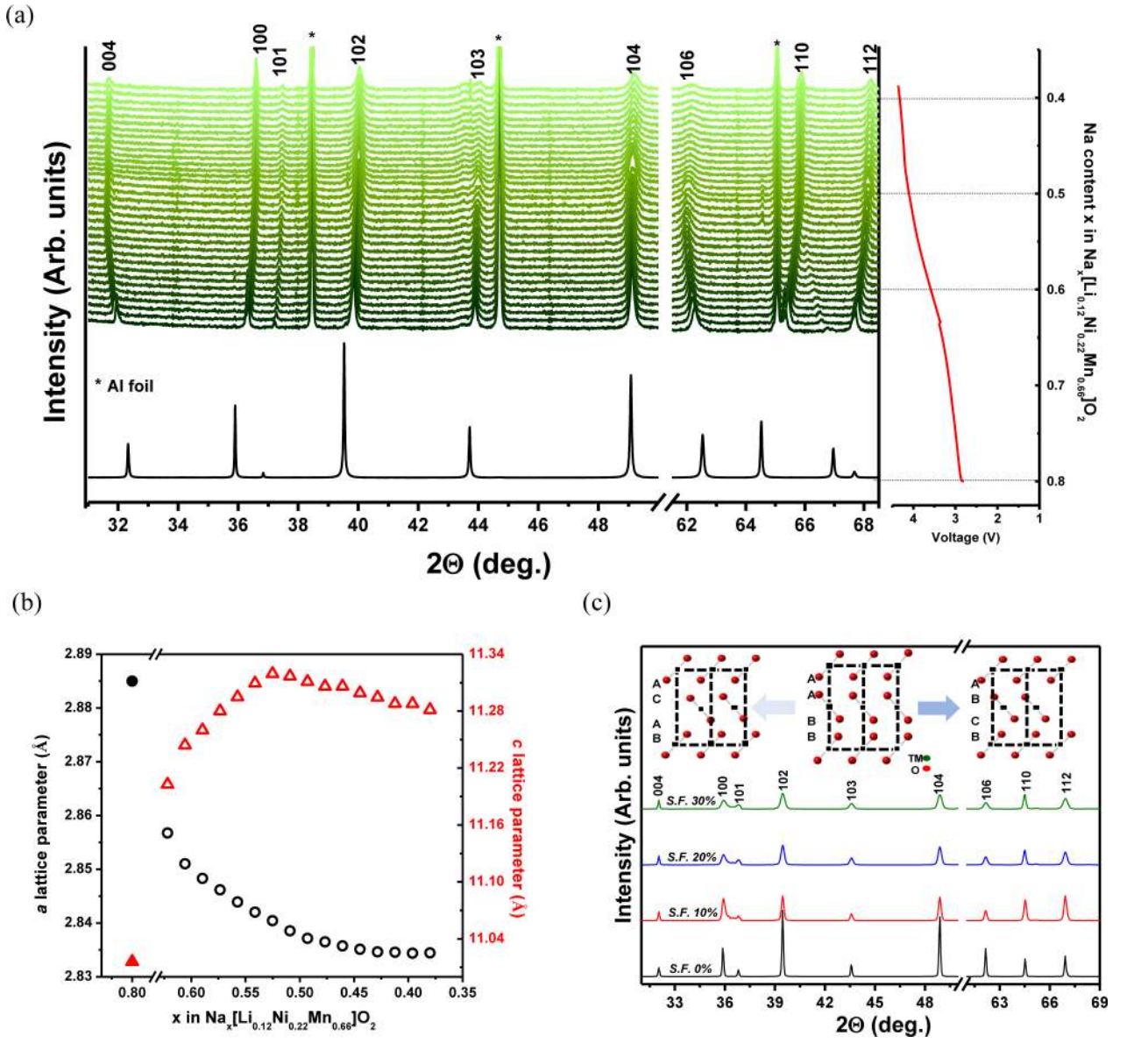

Figure 3. (a) In situ SXRD on $Na_{0.80}[Li_{0.12}Ni_{0.22}Mn_{0.66}]O_2$ during the first charge (peaks marked by "*" are reflections from the Al current collector), (b) evolution of the *a* and *c* lattice parameters during the first charge obtained from Rietveld refinement (solid symbols represent *a* and *c* values in the pristine state), and (c) XRD patterns obtained by simulating different amounts of stacking faults using the CrystalDiffact software.

low Li_6 and Li_7 hyperfine shifts can be rationalized in terms of the smaller number of TM−O-Li connectivities associated with tetrahedral Li, as compared to 6-coordinate Li.

By taking slices along the F2 dimension of the aMAT spectrum (right-hand side of Figure 2b), we can observe the sideband patterns of all distinguishable Li environments in P2−$Na_{0.80}[Li_{0.12}Ni_{0.22}Mn_{0.66}]O_2$. Comparison of the F2 slices reveals a sudden change in the anisotropy of the through space (dipolar) interaction between the Li nucleus and neighboring unpaired TM d-electrons from Li_1 to Li_7. As observed previously, for example, in Li_2MnO_3,[29] ions in the TMO_2 layer (Li_1, Li_2, and Li_3) are expected to have an anisotropy with an opposite sign to that of ions between TM layers (Li_4 and Li_5), confirming their assignments.

The relative population of the Li sites was determined by integration of the 1D Hahn echo spectrum. After correcting for spin−spin relaxation during the NMR pulse sequence, the distribution of Li among the different local environments was found to be: Li_1, 73.5%; Li_2, 11%; Li_3, 2%; Li_4, 5%; Li_5, 3%; Li_6, 5%; Li_7, 0.5%, with an estimated error below ±5%. Detailed information about Li site-specific transversal (spin−spin) relaxation times can be found in Table S6 (Supporting Information). A decrease in Li site population is observed in the aMAT spectrum as the concentration of Ni in the first coordination shell increases. The occupation of Li environments with more than two Ni nearest neighbors is probably too small for these environments to be seen experimentally.

Both neutron diffraction and ^{7}Li NMR data confirm our initial assumption whereby Li^+ primarily occupies octahedral sites in the TMO_2 layer (85% of Li^+ ions are present in the TMO_2 layer according to NMR) and preferentially exchanges with a Ni^{2+} ion. The final Li/Ni/Mn distribution deviates from a simple honeycomb arrangement and exhibits a small amount of Ni/Mn exchange within the TMO_2 layer. ^{7}Li NMR also shows that about 15% of Li^+ ions can be found in O_h/T_d sites in the Na layer.

dx.doi.org/10.1021/cm403855t | *Chem. Mater.* 2014, 26, 1260−1269

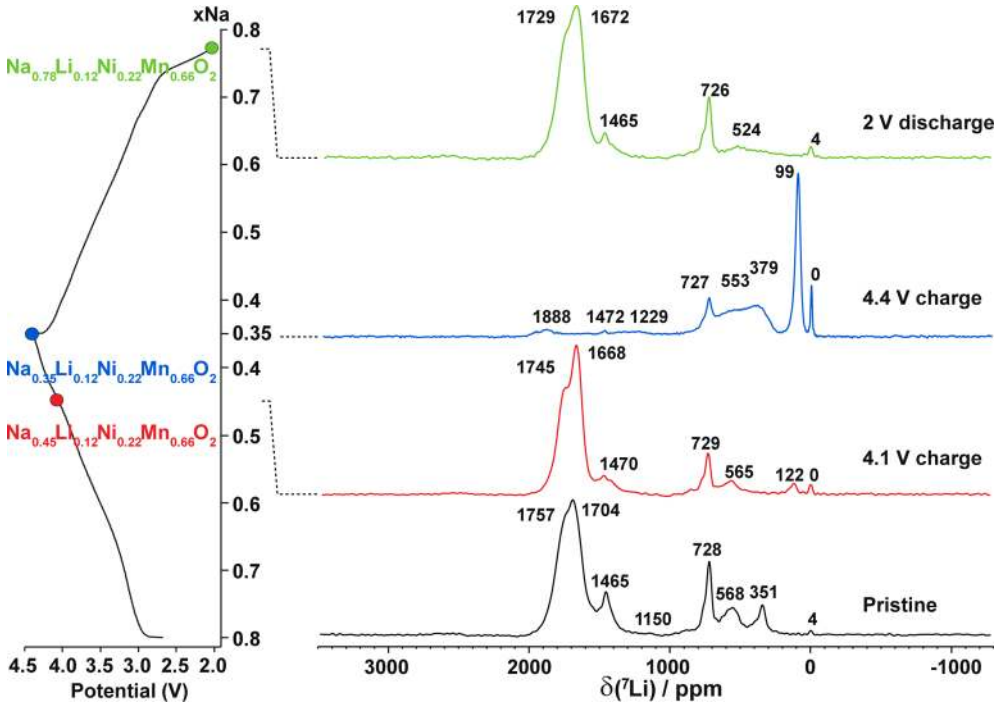

Figure 4. Isotropic slices of ^{7}Li pj-MATPASS NMR spectra acquired at 200 MHz on as-synthesized P2−$Na_{0.8}[Li_{0.12}Ni_{0.22}Mn_{0.66}]O_2$ and at three different stages along the first electrochemical cycle. pj-MATPASS experiments were performed using a train of five nonselective $\pi/2$ pulses. The spectra have not been scaled to represent the total Li content in the sample at each stage of the cycle.

3.3. Structural Evolution during Charge Monitored by in Situ Synchrotron XRD. Phase transformations occurring upon Na-ion extraction were monitored using in situ SXRD. In Figure 3a, selected sections of the SXRD patterns are shown together with the pristine powder pattern at the bottom, and the voltage profile on the right. Refined *a* and *c* lattice parameters, which include the values found in the pristine material, are presented in Figure 3b. The in situ scan was set to start at 3.43 V and end at 4.40 V. Comparison of the whole set of in situ patterns to the pristine powder pattern reveals that all of the major reflections corresponding to the P2 phase are clearly maintained, which demonstrates that no significant phase transformation has occurred. Some of the shifts in peak positions are mainly due to lattice distortions induced by Na-ion extraction. In particular, a gradual shift of the (100) peak toward the high angle end is observed upon charge, in agreement with a decrease in the *a* lattice parameter. Because the *a* lattice parameter corresponds to TM−TM distances, oxidation of TMs upon charge leads to slightly shorter distances between TM. On the other hand, it is obvious that the (004) peak moves toward the low angle end until the cell is charged up to 4.05 V, suggesting an expansion in *c* lattice parameter upon charge due to the increased electrostatic repulsion between successive oxygen layers caused by the removal of Na ions.[32] No noticeable change in the position of the (004) peak can be detected once the voltage has reached 4.05 V. Rietveld refinement suggests a slight decrease in *c* lattice parameter after 4.05 V charge. In the pristine material, Na ions occupy trigonal prismatic sites between neighboring oxygen layers. When some of the Na ions are extracted during charge, TMO_2 slabs glide along the *a*−*b* plane to avoid close oxygen−oxygen contacts. There are two possible directions for these glides (Figure 3c, inset) resulting in a close-packed arrangement of neighboring oxygen layers. Consequently, stacking faults are formed instead of a long-range ordered phase. The presence of these stacking faults within the P2 phase severely broadens (10l) peaks (e.g., (104) and (106)) in the experimental SXRD pattern.[25,33,34] As shown in Figure 3c, such broadening of the XRD pattern due to stacking faults can be simulated using the software CrystalDiffract for Windows 1.4.5.[35,36] An increase in the concentration of stacking faults results in a clear broadening of the (104) and (106) peaks, which is consistent with experimental observations (Figure S2 (a), Supporting Information). Therefore, it is believed that the concentration of stacking faults in the structure progressively increases as the material approaches the end of charge (4.4 V) and accounts for the decrease in *c* lattice parameter after a large amount of Na ions has been removed from the TMO_2 slabs. After one full cycle, complete recovery of the layered P2 structure is confirmed by the presence of sharp, well-defined SXRD peaks at the same positions as those observed for the pristine structure (Figure S2 (b), Supporting Information). The reason for this is the alignment of TM ions along the *c* axis of the P2 structure to form trigonal prismatic Na sites. Hence, when Na ions are reinserted back into the structure, stacking faults are eliminated in such a way that Na-ion prismatic sites can be reconstructed.

3.4. Li Site Change Studied by ex Situ NMR. In Figure 4, ^{7}Li 1D slices are extracted from 2D projection-MATPASS (pj-MATPASS) NMR spectra acquired at 200 MHz on as-synthesized P2−$Na_{0.8}[Li_{0.12}Ni_{0.22}Mn_{0.66}]O_2$ and at 4.1, 4.4 V charge, and 2 V discharge along the first electrochemical cycle. These 1D slices reveal the position of the ^{7}Li isotropic shifts and enable us to monitor changes in ^{7}Li local environments as a function of (dis)charge. Note that the intensity of the peaks in the pj-MATPASS isotropic row of the pristine material (Figure 4) does not match that found in the aMAT F1 sum (Figure 2) spectrum of the same compound as these projections do not

dx.doi.org/10.1021/cm403855t | *Chem. Mater.* 2014, 26, 1260−1269

contain quantitative information on the population of the different Li sites.

While the ^{7}Li NMR spectra at 4.1 V charge and 2 V discharge look very similar to the spectrum of the pristine sample, major changes in the relative occupation of Li local environments occur between 4.1 and 4.4 V on charge. Li site occupations were monitored as a function of cycling by integration of Hahn echo spectra recorded at the four stages of the first cycle mentioned above, and after 5 electrochemical cycles (see Table 1 and Figure S5 of the Supporting Information). Contributions from individual Li sites were scaled by a transverse relaxation factor accounting for the loss of NMR signal intensity over the signal acquisition time.

Table 1. Distribution of Li-Ions between TMO_2 and Na Layer Sites

site	pristine	4.1 V charge	4.4 V charge	2 V discharge	after 5 cycles
TM layer	85	68	5	67	63
Na layer	15	4	38	5	8
total	100	72	43	72	71

The Li content in each layer was obtained by integration of ^{7}Li Hahn echo spectra recorded at the four stages of the first cycle mentioned above, and after 5 electrochemical cycles, and is expressed as a percentage of the total Li content in the pristine phase.

The Li stoichiometry decreases from 0.12 to 0.086 Li per formula unit upon initial charging to 4.1 V, mainly due to the loss of Li in O_h and T_d sites in the Na layer, and, to a smaller extent, to Li loss in the TMO_2 layer. Between 4.1 and 4.4 V charge, the ^{7}Li NMR spectrum changes significantly. Most Li present in TMO_2 layers moves to Na layers, and only 5% of the total Li content in the pristine sample is left in the TMO_2 layer at the end of the first charge. This result can be rationalized using in situ XRD data, which demonstrate the presence of O2-like stacking faults and octahedral (rather than prismatic) sites in the Na layer, inducing Li migration from TMO_2 to Na layers or driven by Li migration. It is difficult to say at this stage if stacking faults enable Li migration or, conversely, if Li-ion mobility facilitates the formation of stacking faults. By the end of charge, most of the Li left in the cathode has moved to O_h, T_d, or other low coordination sites in the Na layer, giving rise to a sharp end-of-charge peak at ca. 100 ppm. The low hyperfine shift may indicate a Ni^{4+}-rich environment, because this cation is diamagnetic (low spin d^0 configuration) and will not contribute to the ^{7}Li Fermi contact shift.

An NMR and first-principles calculations study on O3–$Li[Li_{(1-2x)/3}Mn_{(2-x)/3}Ni_x]O_2$ by Grey et al.[37] showed that the small amount of Li^+-ions occupying octahedral sites in TMO_2 layers participates in the electrochemistry of the cathode by moving spontaneously to a T_d site in Li layers at low potentials, when the four octahedral sites (three in the Li layer and one in the TM layer) that share faces with this T_d site are vacant. A similar scenario may occur in P2–$Na_{0.8}[Li_{0.12}Ni_{0.22}Mn_{0.66}]O_2$, whereby Li directly above a face-sharing Na drops into the space left by Na after the latter is removed during charge and occupies a tetrahedral or trigonal site in the Na layer. This may give rise to a low coordination Li environment, and, if Li is surrounded by a majority of diamagnetic Ni^{4+} ions, account for the 100 ppm NMR resonance.

The Li stoichiometry of the sample, which dropped from 0.086 to 0.051 between 4.1 and 4.4 V charge, increases again to 0.086 by the end of the first discharge. The spectrum at 2 V discharge is very similar to that of the pristine phase, suggesting the reversibility of O2-like stacking faults and of Li migration back to TMO_2 layer sites upon discharge. There is no significant change in total Li content between the end of the first and of the fifth cycles, hence no more irreversible loss of Li in the electrode after the first cycle. The ratio of Li occupation of Na layer sites to that of TMO_2 sites is higher in the pristine phase (ca. 0.08) than in the fully discharged sample (ca. 0.04) and suggests higher reversibility of Li in the transition metal layer than in the Na layer.

3.5. Electronic and Local Structural Changes by XAS.

To investigate charge compensation mechanisms, XAS measurements were conducted at the Ni (8333 eV) and Mn K-edges (6539 eV) at different states of charge (see Figure 5a and Supporting Information Figure S4 (a)). It is evident that the as-synthesized $Na_{0.8}[Li_{0.12}Ni_{0.22}Mn_{0.66}]O_2$ compound predominantly consists of Ni^{2+} and Mn^{4+} ions. The Ni K-edge absorption shifts to a higher energy region when the electrode is charged to 4.1 V, and moves further when the electrode is charged to 4.4 V. The energy shift for the 4.4 V charged electrode is ~3 eV, which is larger than that of the Ni^{2+} to Ni^{3+} shift (~2 eV), suggesting that the oxidation state of Ni is close to Ni^{4+}.[30] After the electrode is discharged to 2.0 V, the Ni-ions

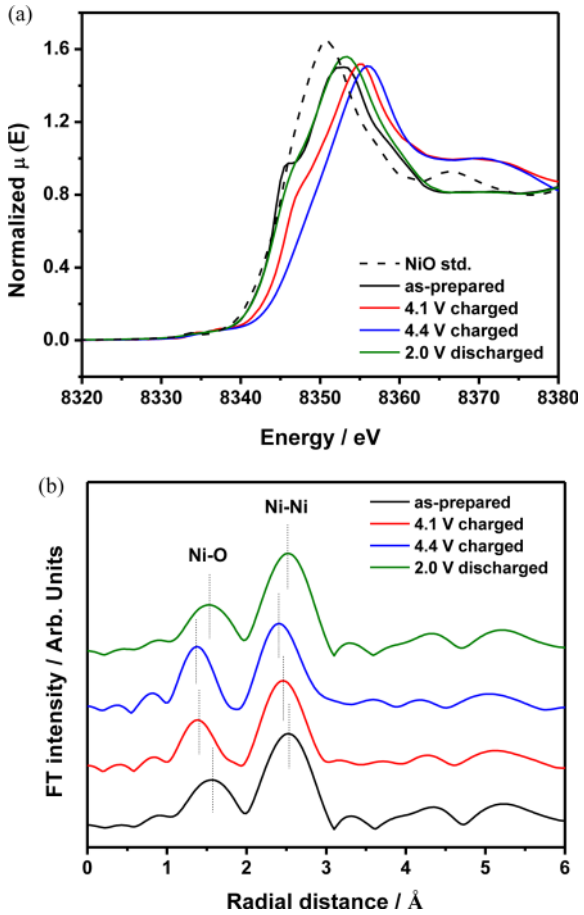

Figure 5. XAS analysis of $Na_{0.8}[Li_{0.12}Ni_{0.22}Mn_{0.66}]O_2$ charged to 4.1, 4.4 V and discharged to 2.0 V at the Ni K-edge (a) XANES region including a NiO standard and (b) the EXAFS spectra.

dx.doi.org/10.1021/cm403855t | Chem. Mater. 2014, 26, 1260–1269

return back to their divalent state, demonstrating that the Ni redox reaction is completely reversible in the Na-ion cell. In contrast to the Ni XANES, Mn stays in its tetravalent state during charge and discharge (see Supporting Information Figure S4 (a)). On the basis of the reversible capacity shown in Figure 1a, 0.44 mol of Na-ions per formula unit migrates upon cycling, delivering 118 mAh g^{-1} of capacity. This means that all Ni^{2+} ions present in the pristine phase are fully oxidized to Ni^{4+} to balance the overall charge of the system.

Extended X-ray absorption fine structure (EXAFS) spectra were further analyzed. As shown in Figure 5b, the Ni EXAFS clearly shows that the Ni−O interatomic distance, around 1.5 A in the pristine phase, decreases upon charge due to the oxidation of Ni^{2+} to Ni^{4+}. The Ni−O distance reverts back to its initial value by the end of the first discharge, in good agreement with XANES results. On the other hand, the Mn EXAFS does not show any obvious changes in the Mn−O interatomic distance. The XAS proves that Ni is the only electrochemically active species and Mn maintains the structural stability in the absence of Jahn−Teller active Mn^{3+}.

3.6. The Role of Li Substitution in $Na_{0.8}[Li_{0.12}Ni_{0.22}Mn_{0.66}]O_2$. The sites substituted by Li in the as-synthesized $Na_{0.8}[Li_{0.12}Ni_{0.22}Mn_{0.66}]O_2$ compound were identified by using both NMR and neutron diffraction. Although a small amount of Li ions can be found in octahedrally coordinated Na layer sites, presumably as a result of O-type defects (ABCABC or ABAB oxygen stacking[38]), most Li-ions are not stable in the large prismatic Na sites and occupy TM sites. As expected, Li-ions preferentially occupy TM sites with a high number of nearest neighbor Mn^{4+} ions (4, 5, or 6). This suggests that they preferentially replace Ni^{2+} ions in the TMO_2 layer, because the monovalent Li^+ ion can reduce in-plane electrostatic repulsion between cations as well as disrupt the cation orderings. As opposed to Li-free P2 cathodes, single smooth voltage curves are obtained rather than step-like electrochemical profiles, suggesting that no significant structural changes occur during cycling. Rather than a P2−O2 phase transformation, in situ SXRD suggests the presence of local O2-like stacking faults at the end of charge. The presence of stacking faults has also been confirmed by ex situ NMR, which reveals a 5-fold increase in the occupation of octahedral Na layer sites by Li between 4.1 and 4.4 V charge.

The effect of Li substitution upon the electrode's electrochemical performance was studied by charging the cell using constant current constant voltage (CCCV) to pull all of the Na ions out (0.80 mols of Na ions per formula unit) below 4.4 V, to avoid electrolyte decomposition. After all Na ions were extracted from the structure, the O2 phase was clearly observed in ex situ XRD (Figure S3, Supporting Information), demonstrating that the P2−O2 phase transformation is delayed instead of being completely prevented. In other words, the O2 phase forms inevitably once all Na-ions are removed from the P2 phase. Therefore, the main characteristics of Li substitution and their possible consequences on phase transformation can be summarized as follows. Li ions prefer to occupy octahedrally coordinated sites in the TMO_2 layer with a high number of Mn nearest neighbor atoms; concurrently, the lower valence state of Li ions (monovalent) as compared to that of Ni ions (divalent) requires more Na ions to be inserted in the as-synthesized material to maintain the overall charge balance of the compound. As a result, approximately 0.36 mol of Na ions is left in prismatic sites after 4.4 V charge, which is enough to suppress the O2 phase transformation. Although Li ions in substituted TM sites migrate to octahedral sites or to tetrahedral sites in the Na layer created by local stacking faults, the amount of Li in the TM layer in the cycled electrode is largely recovered, suggesting that the migration of Li between octahedral sites in the Na layer and in the TM layer is highly reversible. We note that a fraction of Li is lost on the first cycle but that little seems to be lost in subsequent cycles. The excellent reversibility of Li migration of the remaining Li in this compound may account for its excellent capacity retention and its single smooth voltage curves throughout the whole cycling process.

3.7. Material Design Principles and $Na_{0.83}[Li_{0.07}Ni_{0.31}Mn_{0.62}]O_2$. To achieve both high-energy density and structural stability, the stoichiometry of Li-substituted P2 type cathodes can be further optimized. The above discussion, which focused on the crystallographic and electronic structural changes occurring upon cycling $Na_{0.8}[Li_{0.12}Ni_{0.22}Mn_{0.66}]O_2$, has led to the identification of several key conditions which need to be fulfilled for good electrochemical performance in P2 type cathodes. Here, we propose novel principles for the design of positive electrodes to obtain higher energy density cathode materials with stoichiometry $Na_x[Li_yNi_zMn_{1-y-z}]O_2$ ($0 < x, y, z < 1$). First, an increase in Na-ion concentration in the structure is required to deliver higher energy density and to maintain the P2 phase up to the end of charge. However, Na concentration in the as-synthesized material cannot be higher than 0.9 per formula unit if the extremely unfavorable simultaneous occupancy of nearest-neighbor Na sites in the P2 structure is to be prevented.[10,39,40] Second, a high proportion of Ni ions in the TM layer is essential to provide enough electrons via the oxidation of Ni^{2+} to Ni^{4+} for high voltage electrochemical processes. Third, the Ni to Mn ratio significantly affects the phase of the synthesized product. The highest ratio we can achieve is 1:2, and a further increase in Ni-ion concentration leads to the formation of impurities including transition metal oxides, or O3 phases. Fourth, overall charge balance of the compound has to be taken into account. The algebraic relationship between the x, y, and z stoichiometric factors in the $Na_x[Li_yNi_zMn_{1-y-z}]O_2$ formula is given by

$$x + y + 2 \times z + 4 \times (1 - y - z) = 2 \times 2 \quad (1)$$

$$x < 0.9 \quad (2)$$

$$1 - y - z = 2 \times z \quad (3)$$

$$0 < x, y, z < 1 \quad (4)$$

We suggest an optimum composition, which fulfills all of the above conditions, in which $x = 3 - 7z$, $y = 1 - 3z$, and $0.3 < z < 0.33$. A novel composition, $Na_{0.83}[Li_{0.07}Ni_{0.31}Mn_{0.62}]O_2$, is finally obtained, which can deliver 140 mAh g^{-1} of reversible capacity in the voltage range of 2.0−4.4 V (Figure 6). The stoichiometry was confirmed by ICP. As expected, no significant phase transformation was observed upon cycling based on our preliminary in situ XRD studies, except for a slight change in the voltage curves shown repeatedly in the high voltage region. This change may be the result of the formation of intermediate phases through Na-ion ordering.[39,41] An in-depth study of Na-ion ordering this family of materials is currently in progress.

dx.doi.org/10.1021/cm403855t | Chem. Mater. 2014, 26, 1260−1269

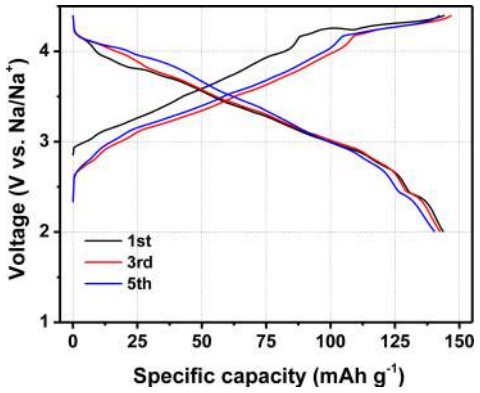

Figure 6. Electrochemical profiles of $Na_{0.83}[Li_{0.07}Ni_{0.31}Mn_{0.62}]O_2$ in the voltage range of 2.0−4.4 V during the 1st, 3rd, and 5th cycles.

4. CONCLUSIONS

An in-depth understanding of the interplay between structural properties and electrochemical performances is required to improve the performances of Na-ion batteries. In this work, a promising Na cathode material, P2−$Na_{0.8}[Li_{0.12}Ni_{0.22}Mn_{0.66}]O_2$, has been comprehensively studied using neutron diffraction, ^{7}Li solid-state MAS NMR, in situ SXRD, and XAS. Most of the substituted Li ions occupy TM sites with a high number of nearest-neighbor Mn ions (4, 5, or 6), a result confirmed by both neutron diffraction and NMR. Enhanced electrochemical properties, among which improved cycling performance and rate capability, are obtained along with single smooth voltage profiles. In contrast to most of the P2-type cathodes reported so far, in situ SXRD proves that the frequently observed P2−O2 phase transformation is inhibited in this Li-substituted material even when the electrode is charged to 4.4 V. On the other hand, the P2 to O2 phase change is clearly observed when all of the Na ions are extracted from the structure under CCCV charge. On the basis of these observations, Li substitution in the TM layer enables enough Na ions to be left in the structure to maintain the P2 structure up to 4.4 V charge. Although Li ions migrate to octahedral or, to a lesser extent, to low coordination sites in the Na layer formed by local stacking faults during the charging process, most of them return to the TM layer after discharge. XAS results show that Ni^{2+}/Ni^{4+} is the only active redox couple during cycling. Finally, an optimum composition, $Na_{0.83}[Li_{0.07}Ni_{0.31}Mn_{0.62}]O_2$, has been proposed on the basis of the design principles for Na-ion cathode elucidated as part of this study, opening new perspectives for further exploration of high-energy Na-ion batteries.

■ ASSOCIATED CONTENT

Ⓢ Supporting Information

Additional figures and tables (PDF). This material is available free of charge via the Internet at http://pubs.acs.org.

■ AUTHOR INFORMATION

Corresponding Author

*Tel.: (858) 822-4247. Fax: (858) 534-9553. E-mail: shirleymeng@ucsd.edu.

Author Contributions

⊥These authors contributed equally.

Notes

The authors declare no competing financial interest.

■ ACKNOWLEDGMENTS

We acknowledge support from the National Science Foundation under Award Number 1057170. The neutron diffraction was conducted at Oak Ridge National Laboratory on POWGEN beamline by mail-in program. The ex situ synchrotron X-ray diffraction patterns were collected at Argonne National Laboratory on beamline 11-BM through the general user proposal mail-in program. NMR experiments at 500 MHz field were conducted at the Centre de Résonance Magnétique Nucléaire à Très Hauts Champs (CRMN), Institut des Sciences Analytiques, Villeurbanne, France. We thank Prof. Lyndon Emsley many helpful discussions concerning the NMR experiments. NMR experiments at 200 MHz field were performed at the University of Cambridge, Cambridge, UK. R.J.C. acknowledges support from the European Research Council (ERC). M.L. thanks the EU Marie Curie intra-European fellowship for funding. A.J.P. was supported by the LABEX iMUST (ANR-10-LABX-0064) of the Université de Lyon, within the program "Investissements d'Avenir" (ANR-11-IDEX-0007) operated by the Agence Nationale de la Recherche (ANR). X.Y. and X.-Q.Y. were supported by the U.S. Department of Energy, the Assistant Secretary for Energy Efficiency and Renewable Energy, Office of Vehicle Technologies under Contract Number DEAC02-98CH10886. The technical support from beamline scientists at X11B and X14A of NSLS is gratefully acknowledged.

■ REFERENCES

(1) Yang, Z. G.; Zhang, J. L.; Kintner-Meyer, M. C. W.; Lu, X. C.; Choi, D. W.; Lemmon, J. P.; Liu, J. *Chem. Rev.* **2011**, *111*, 3577−3613.
(2) Komaba, S.; Takei, C.; Nakayama, T.; Ogata, A.; Yabuuchi, N. *Electrochem. Commun.* **2010**, *12*, 355−358.
(3) Komaba, S.; Nakayama, T.; Ogata, A.; Shimizu, T.; Takei, C.; Takada, S.; Hokura, A.; Nakai, I. *ECS Trans.* **2009**, *16*, 43−55.
(4) Rudola, A.; Saravanan, K.; Mason, C. W.; Balaya, P. *J. Mater. Chem. A* **2013**, *1*, 2653−2662.
(5) Senguttuvan, P.; Rousse, G.; Seznec, V.; Tarascon, J.-M.; Palacín, M. R. *Chem. Mater.* **2011**, *23*, 4109−4111.
(6) Delmas, C.; Fouassier, C.; Hagenmuller, P. *Physica B & C* **1980**, *99*, 81−85.
(7) Fouassier, C.; Delmas, C.; Hagenmuller, P. *Mater. Res. Bull.* **1975**, *10*, 443−449.
(8) Delmas, C.; Braconnier, J.-J.; Fouassier, C.; Hagenmuller, P. *Solid State Ionics* **1981**, *3*, 165−169.
(9) Xu, J.; Lee, D. H.; Meng, Y. S. *Funct. Mater. Lett.* **2013**, *6*, 1330001.
(10) Berthelot, R.; Carlier, D.; Delmas, C. *Nat. Mater.* **2011**, *10*, 74−80.
(11) Lu, Z. H.; Dahn, J. R. *J. Electrochem. Soc.* **2001**, *148*, A710−A715.
(12) Lu, Z.; Dahn, J. R. *J. Electrochem. Soc.* **2001**, *148*, A1225−A1229.
(13) Yabuuchi, N.; Kajiyama, M.; Iwatate, J.; Nishikawa, H.; Hitomi, S.; Okuyama, R.; Usui, R.; Yamada, Y.; Komaba, S. *Nat. Mater.* **2012**, *11*, 512−517.
(14) Kim, D.; Kang, S.-H.; Slater, M.; Rood, S.; Vaughey, J. T.; Karan, N.; Balasubramanian, M.; Johnson, C. S. *Adv. Energy Mater.* **2011**, *1*, 333−336.
(15) Toby, B. H. *J. Appl. Crystallogr.* **2001**, *34*, 210−213.
(16) Clement, R. J.; Pell, A. J.; Middlemiss, D. S.; Strobridge, F. C.; Miller, J. K.; Whittingham, M. S.; Emsley, L.; Grey, C. P.; Pintacuda, G. *J. Am. Chem. Soc.* **2012**, *134*, 17178−17185.
(17) Hung, I.; Zhou, L. N.; Pourpoint, F.; Grey, C. P.; Gan, Z. H. *J. Am. Chem. Soc.* **2012**, *134*, 1898−1901.
(18) Jian Zhi, H.; Alderman, D. W.; Chaohui, Y.; Pugmire, R. J.; Grant, D. M. *J. Magn. Reson., Ser. A* **1993**, *105*, 82−87.

(19) Hwang, T. L.; van Zijl, P. C. M.; Garwood, M. *J. Magn. Reson.* **1998**, *133*, 200−203.
(20) Kervern, G.; Pintacuda, G.; Emsley, L. *Chem. Phys. Lett.* **2007**, *435*, 157−162.
(21) Massiot, D.; Fayon, F.; Capron, M.; King, I.; Le Calve, S.; Alonso, B.; Durand, J. O.; Bujoli, B.; Gan, Z. H.; Hoatson, G. *Magn. Reson. Chem.* **2002**, *40*, 70−76.
(22) Newville, M. *J. Synchrotron Radiat.* **2001**, *8*, 322−324.
(23) Ravel, B.; Newville, M. *J. Synchrotron Radiat.* **2005**, *12*, 537−541.
(24) Kim, D.; Kang, S. H.; Slater, M.; Rood, S.; Vaughey, J. T.; Karan, N.; Balasubramanian, M.; Johnson, C. S. *Adv. Energy Mater.* **2011**, *1*, 333−336.
(25) Lu, Z.; Dahn, J. R. *J. Electrochem. Soc.* **2001**, *148*, A1225−A1229.
(26) Lu, Z.; Donaberger, R. A.; Dahn, J. R. *Chem. Mater.* **2000**, *12*, 3583−3590.
(27) Meng, Y. S.; Ceder, G.; Grey, C. P.; Yoon, W. S.; Jiang, M.; Breger, J.; Shao-Horn, Y. *Chem. Mater.* **2005**, *17*, 2386−2394.
(28) Kim, J.; Middlemiss, D. S.; Chernova, N. A.; Zhu, B. Y. X.; Masquelier, C.; Grey, C. P. *J. Am. Chem. Soc.* **2010**, *132*, 16825−16840.
(29) Grey, C. P.; Dupre, N. *Chem. Rev.* **2004**, *104*, 4493−4512.
(30) Yoon, W. S.; Iannopollo, S.; Grey, C. P.; Carlier, D.; Gorman, J.; Reed, J.; Ceder, G. *Electrochem. Solid-State Lett.* **2004**, *7*, A167−A171.
(31) Cabana, J.; Chernova, N. A.; Xiao, J.; Roppolo, M.; Aldi, K. A.; Whittingham, M. S.; Grey, C. P. *Inorg. Chem.* **2013**, *52*, 8540−8550.
(32) Carlier, D.; Cheng, J. H.; Berthelot, R.; Guignard, M.; Yoncheva, M.; Stoyanova, R.; Hwang, B. J.; Delmas, C. *Dalton Trans.* **2011**, *40*, 9306.
(33) Zhonghua, L.; Dahn, J. R. *Chem. Mater.* **2001**, *13*, 2078−2083.
(34) Tournadre, F.; Croguennec, L.; Saadoune, I.; Carlier, D.; Shao-Horn, Y.; Willmann, P.; Delmas, C. *J. Solid State Chem.* **2004**, *177*, 2790−2802.
(35) Mueller, T.; Ceder, G. *Phys. Rev. B* **2010**, *82*, 7.
(36) Jiang, X.; Århammar, C.; Liu, P.; Zhao, J.; Ahuja, R. *Sci. Rep.* **2013**, 3.
(37) Grey, C. P.; Yoon, W. S.; Reed, J.; Ceder, G. *Electrochem. Solid-State Lett.* **2004**, *7*, A290−A293.
(38) Paulsen, J. M.; Donaberger, R. A.; Dahn, J. R. *Chem. Mater.* **2000**, *12*, 2257−2267.
(39) Lee, D. H.; Xu, J.; Meng, Y. S. *Phys. Chem. Chem. Phys.* **2013**, *15*, 3304−3312.
(40) Guignard, M.; Didier, C.; Darriet, J.; Bordet, P.; Elkaim, E.; Delmas, C. *Nat. Mater.* **2013**, *12*, 74−80.
(41) Berthelot, R.; Carlier, D.; Delmas, C. *Nat. Mater.* **2011**, *10*, 74−U3.